JGR Space Physics

Key Points:
- Level 2 data of China Seismo-Electromagnetic Satellite high precision magnetometer (HPM) payload are introduced and explained, for users interested in using this data set
- A preliminary comparison with Swarm data shows that this HPM data is of good quality
- An example study of an intense geomagnetic storm suggests that the HPM data has a high scientific potential

Correspondence to:
X. Shen,
shenxh@seis.ac.cn

CSES High Precision Magnetometer Data Products and Example Study of an Intense Geomagnetic Storm

Yanyan Yang[1,2] , Bin Zhou[3], Gauthier Hulot[4], Nils Olsen[5] , Yingyan Wu[6] , Chao Xiong[7,8], Claudia Stolle[8] , Zeren Zhima[1,2] , Jianping Huang[1,2], Xinghong Zhu[9], Andreas Pollinger[10], Bingjun Cheng[3], Werner Magnes[10] , Xudong Zhao[11], and Xuhui Shen[1,2]

[1]National Institute of Natural Hazards, Ministry of Emergency Management of China, Beijing, China, [2]Center for Satellite Application in Earthquake Science, China Earthquake Administration, Beijing, China, [3]National Space Science Center, Chinese Academy of Sciences, Beijing, China, [4]Université de Paris, Institut de Physique du Globe de Paris, CNRS, Paris, France, [5]DTU Space, National Space Institute, Technical University of Denmark, Copenhagen, Denmark, [6]Institute of Earthquake Forecasting, China Earthquake Administration, Beijing, China, [7]Department of Space Physics, Electronic Information School, Wuhan University, Wuhan, China, [8]GFZ German Research Centre for Geosciences, Potsdam, Germany, [9]DFH Satellite Co. Ltd., Beijing, China, [10]Space Research Institute, Austrian Academy of Sciences, Graz, Austria, [11]Institute of Geophysics, China Earthquake Administration, Beijing, China

Abstract Providing accurate measurement of the magnetic field intensity and its vector components is one of the primary objectives of the China Seismo-Electromagnetic Satellite (CSES). The high precision magnetometer (HPM) payload assembled on CSES is designed to achieve this goal. In this study, the data format, naming convention, and content of the CSES HPM Level 2 scientific data products are introduced, as a reference for users who are interested in this data set. In particular, flags for potential magnetic field disturbances from the platform and payloads are discussed. Possible scientific applications are also outlined. A preliminary validation of the data is conducted through comparison with magnetic data from the ESA's Swarm constellation, and the result demonstrates that the HPM data of CSES are of good quality. Taking the intense geomagnetic storm that occurred on August 25–26, 2018 as an example, the magnetic field variations and the expansion of the field-aligned currents (FACs) during this storm are discussed. We finally show that the CSES HPM data can be used to derive a satellite-derived index equivalent to the *Dst* index, which agrees well to the index during this event. Our analysis thus suggests a high scientific potential of the HPM data.

1. Introduction

The China Seismo-Electromagnetic Satellite (CSES, Shen et al., 2018), also named ZH-1, was successfully launched on February 2, 2018 on a near polar Sun-synchronous (ascending/descending local times of 02:00/14:00) orbit with an initial altitude of 507 km and an inclination of 97.4°. It has a 5-day revisiting period and the orbit distribution during a whole revisiting period from August 26–30, 2018 is shown in Figure 1. Eight scientific instruments are assembled on CSES, to obtain measurements of the magnetic field, the electric field and plasma parameters. Accurate measurements of the magnetic field are carried out by the high precision magnetometer (HPM, Cheng et al., 2018) package. This HPM package comprises a dual fluxgate magnetometer (FGM) and one coupled dark state magnetometer (CDSM, Pollinger et al., 2018), which respectively measure the magnetic vector components (from DC to 15 Hz) and scalar values (from DC to 0.5 Hz). The two FGM instruments on CSES were switched on three days after the launch of the satellite, while the CDSM instrument started to operate at the beginning of March 2018. The HPM payload has since been operated continuously and is in good health.

The geomagnetic field is an essential parameter for space science studies. Many phenomena can be studied using magnetic field observations. Magnetic measurements from space began with the satellite era and the launch of Sputnik 3 in 1958 (Dolginov et al., 1962). At low Earth orbits (LEO), progress was next gradually achieved from a series of missions, for example, POGO, Magsat (Langel et al., 1982), Ørsted (Neubert et al., 2001), CHAMP (Reigber et al., 2002), SAC-C and Swarm (Friis-Christensen et al., 2006). Exploration of Earth's magnetic field has always been at the forefront of science and applications.
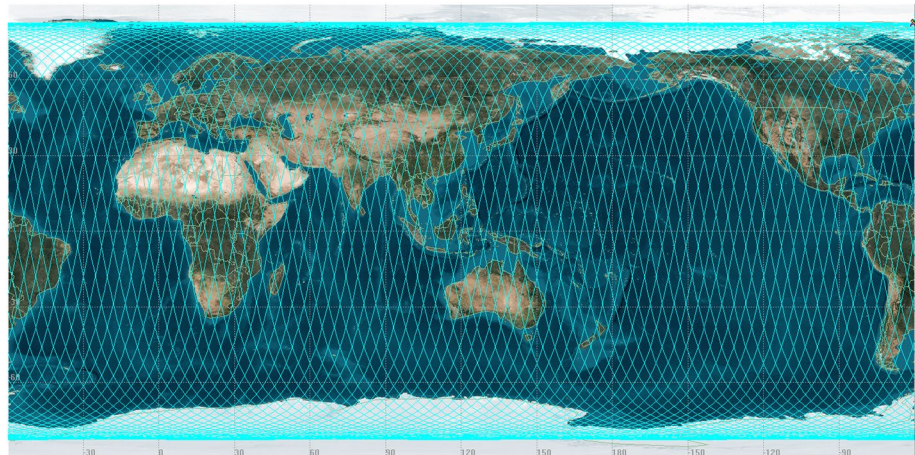
Figure 1. China Seismo-Electromagnetic Satellite (CSES) orbit distribution for a whole revisiting period during July 26–30, 2018.

At LEO satellite altitude, the intensity of the magnetic field varies from about 20,000 nT (in the equatorial region) to 65,000 nT (over the poles). It is the result of both internal and external field contributions (see, e.g., Hulot et al., 2015). The internal field is the dominant part (about 98%–99% of the total field at ground level). It originates mainly from dynamo effects in the Earth's fluid outer core and from magnetized material in the crust. The weaker but more dynamic external field is the result of contributions from various electric current systems in the ionosphere and magnetosphere. Mathematically, the internal and external field can be described by a series of spherical harmonic functions (ignoring the magnetic field due to in situ electric currents at satellite altitude). A typical model of the main field is the International Geomagnetic Reference Field (IGRF, Thébault et al., 2015), which describes the internal field produced by the core up to spherical harmonic degree 13, corresponding to spatial scales larger than about 3,000 km on ground. The crustal field dominates at higher spherical harmonic degrees. Models that include higher degrees of spherical harmonics to further account for this field are also available, for example, the CHAOS (e.g., Finlay et al., 2016; Olsen et al., 2006), GRIMM (Lesur et al., 2008), and POMME (Maus et al., 2006) geomagnetic field models.

Despite the availability of many magnetic field measurements and models, more data are always needed to monitor the temporal evolution of the core field with improved spatial resolution. Of special importance are simultaneous observations taken by several satellites, as demonstrated by the three LEO satellites of the ESA Swarm mission (Friis-Christensen et al., 2006). ESA approved the continuous operation of this mission – launched in November 2013 – until at least the end of 2022. All three satellites and their payload are in excellent condition and ready for operation for even more years. CSES and Swarm therefore have a good chance to operate simultaneously in the coming years. The combined constellation of CSES and Swarm offers the possibility of simultaneous four-point measurements of the magnetic field in LEO, which can greatly enhance the scientific scopes addressed by either mission on its own. For example, simultaneous measurements at different altitudes and local times will allow a better separation of internal and external contributions of the magnetic field. Furthermore, the difference of orbital inclination of the two missions (CSES: 97.4°, Swarm Alpha and Charlie: 87.4°, Swarm Bravo: 88°) results in different local time samplings, thereby improving spatial and temporal resolutions.

The purpose of this study is to provide detailed information about the CSES HPM data and capabilities of the payload. In the following, we will first give a description of the HPM Level 2 scientific (calibrated) data product. Then, a series of comparison of magnetic field observations taken by the two CSES and Swarm missions are conducted taking advantage of CSES-Swarm conjunctions. Finally, the magnetic field response during an intense geomagnetic storm event is investigated to further illustrate the potential of HPM measurements for scientific research.
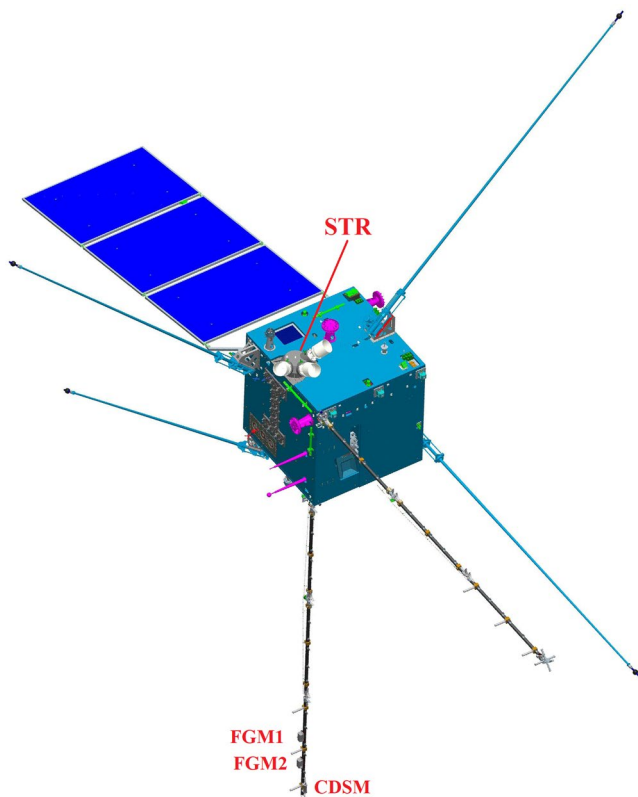
Figure 2. Sketch of the CSES satellite with location of the high precision magnetometer package.

2. The HPM Payload and Its Calibrated Level 2 Data

The HPM sensors are mounted on one of the six booms of the spacecraft while the electronics unit is installed in the satellite platform. Figure 2 shows the HPM sensor positions on the satellite. The length of the boom is about 5 m. HPM includes two FGM fluxgate magnetometers and one CDSM scalar instrument with low absolute error (for more details, see Cheng et al., 2018; Pollinger et al., 2018). The two FGM instruments, manufactured by National Space Science Center, Chinese Academy of Sciences, measure the magnetic field vector with a sampling rate of 60 Hz. In principle, either of the two FGM sensors can be used as primary sensor for the main data stream. In normal operation, the FGM2 sensor, located further away from the platform, is used as the main data source for the calibrated Level 2 products. In the studies presented here, only FGM2 data were used for all calculations. The CDSM instrument provides measurements of the magnetic field intensity with an update rate of 1 Hz and is used for in-flight calibration of the vector components obtained by the two FGM instruments. The CDSM was developed by the Space Research Institute of the Austrian Academy of Sciences and the Institute of Experimental Physics of the Graz University of Technology (see Pollinger et al., 2018).

The calibration of HPM data includes the transformation from the raw telemetry data in binary units to magnetic vector components in physical units of nT in the NEC (North East Center) geographic coordinate system. The processing involves a calibration model of pre-flight calibration parameters and additional parameters determined during the in-flight calibration process. These parameters, as well as the calibration model and main results, have been described in Cheng et al. (2018), B. Zhou et al. (2018, 2019), and Pollinger et al. (2020). Here, we only provide a general description of the method presently used (note, indeed, that the method is likely to be improved throughout the mission lifetime). The calibration of HPM includes four main steps. First, the FGM and CDSM raw signals are converted to the physical quantity according to their principle. Calibration parameters used in this process have been determined on ground before the launch of the satellite. Second, the scalar values of CDSM are used to calibrate the linear parameters of the FGM in orbit, that is, orthogonalization of the FGM. These linear parameters are calculated separately for the day and nightside and updated every day. Third, interferences from satellite and other sensors are further removed. The fourth and final step of the calibration consists in the rotation of the coordinate system from the FGM sensor frame to the NEC frame. This is done using successive rotations. We first rotate data from the FGM sensor frame to the STR frame (which is not mounted on the boom but on the body of the satellite, see Figure 2). The Euler angles describing this rotation are optimized by comparing the data in the final NEC frame with predictions from the CHAOS-6 (Finlay et al., 2016) model. These angles are updated every day, separately for day and nightsides. The magnetic field vector is next further rotated from STR frame to Earth-centered inertial (ECI), then to Earth-centered Earth-fixed (ECEF) coordinate system and finally to the NEC frame.

The HPM Level 2 data products, which are stored in the Hierarchical Data Format (HDF5), include the final calibrated physical quantities on orbital segment basis, that is, each product contains all available data of a descending or an ascending orbit segment. The naming convention for HPM Level 2 data is:

CSES_01_HPM_<apid>_<level>_<para_code>_<orbit>_<start_time>_<end_time>_< station>.h5

- <apid>: payload ID, 4 for FGM1, 5 for FGM2 and 6 for CDSM
- <level>: levels of the data produce, from L00 to L04. The calibrated data is L02
- <para_code>: parameter code, A2 for the magnetic field
- <orbit>: orbit number, 6 digital numbers, the last digit: 1 for ascending and 0 for descending orbit

Table 1
FGM and CDSM Level 2 Data File Attribute

Element	Description
SOFTVERSION	Software version
PAYLOADID	Instrument code. HPM is 146F0101
ORBITNUM	Orbit number
ORBITTYPE	Orbit type. 1: ascending orbit, 0: descending orbit
SAMPLERATE	Sampling rate, 1 Hz
FREQRANGE	Frequency range, DC~0.5 Hz

- <start_time>: UTC time of the first data point in format of YYYYMMDD_HHMMSS
- <end_time>: UTC time of the last data point in format of YYYYMMDD_HHMMSS
- <station>: the ground receiver station code, 3 digital numbers

An example file name for CSES HPM Level 2 data from the FGM2 instrument, on the ascending part of orbit number 10137, starting on December 1, 2019 at 03 h 30 min 16 s and ending on the same day at 04 h 08 min 20 s, received by station 000, is:

CSES_01_HPM_5_L02_A2_101371_20191201_033016_20191201_040820_000.h5

The Level 2 data products from the three sensors FGM1, FGM2, CDSM of the HPM package are separately stored. Tables 1–3 show the attribute and data products content for the FGM and CDSM files. Generally, the FGM file provides magnetic vector field components in both the NEC and FGM frame while the CDSM file gives the magnetic field intensity. From the NEC frame, it is very easy to transform to the spherical coordinates by:

$$\left(B_r, B_\theta, B_\varphi\right)_{\text{GEO}} = \left(-B_C, -B_N, B_E\right)_{\text{NEC}} \quad (1)$$

In addition, both Level 2 FGM and CDSM data products include information such as the spacecraft position (altitude relative to Earth's mean radius 6,371.2 km, geographic latitude and longitude, geomagnetic latitude and longitude based on dipole coordinates using IGRF-12 (Thébault et al., 2015), with 1 day accuracy) and observation time (UTC time and verse time, i.e., the relative time (in ms) since 00:00:00 of January 1, 2009). Quality flags are also provided with the products. For FGM, three flags, that is, FLAG_MT, FLAG_SHW, and FLAG_TBB are used to respectively denote the magnetic disturbances produced by the magnetorquer action, by the boom deformation when entering in the shadow, and due to the Tri-Band Beacon (TBB) payload. For CDSM, in addition to FLAG_MT, FLAG_N3 is added to distinguish two working modes $N = 2$ and $N = 3$. The CDSM, indeed, is an optical scalar magnetometer based on a quantum interference effect called coherent population trapping (CPT). The instrument is inherently omnidirectional, taking advantage of two different resonance superpositions arising at different angles between the sensor

Table 2
Content of FGM Level 2 Data Products

Element	Content	Units
A221	North component of magnetic field in the NEC frame	nT
A222	East component of magnetic field in the NEC frame	nT
A223	Center component of magnetic field in the NEC frame	nT
ALTITUDE	Altitude relative to Earth's mean radius (6,371.2 km)	km
B_FGM	Three components of magnetic field vector in FGM frame	nT
FLAG_MT	Flag to signal disturbance from magnetorquer. 1: disturbed; 0: not disturbed	–
FLAG_SHW	Flag to signal entering of ground shadow. 1: entering ground shadow; 0: sunlight region	–
FLAG_TBB	Flag to signal disturbance from Tri-Band Beacon (TBB). 1: disturbed; 0: not disturbed	–
GEO_LAT	Geographic latitude	degree
GEO_LON	Geographical longitude	degree
MAG_LAT	Geomagnetic latitude	degree
MAG_LON	Geomagnetic longitude	degree
UTC_TIME	UTC time, format: YYYYMMDDHHMMSSFFF	–
VERSE_TIME	Relative time from 00:00:00 of January 1, 2009	ms
q_SIM_ECI	Quaternion parameters describing the rotation from star imager frame to Earth-centered inertial (ECI) frame	–

Table 3
Content of CDSM Level 2 Data Products

Element	Content	Units
A211	Scalar magnetic field data from CDSM	nT
ALTITUDE	Altitude relative to Earth's mean radius (6,371.2 km)	km
FLAG_MT	Flag to signal disturbance from magnetorquer. 1: disturbed; 0: not disturbed	–
FLAG_N3	Flag to signal the working mode of CDSM. 1: $N = 3$; 0: $N = 2$	–
GEO_LAT	Geographic latitude	degree
GEO_LON	Geographical longitude	degree
MAG_LAT	Geomagnetic latitude	degree
MAG_LON	Geomagnetic longitude	degree
UTC_TIME	UTC time, format: YYYYMMDDHHMMSSFFF	–
VERSE_TIME	Relative time from 00:00:00 of January 1, 2009	ms

and the magnetic field vector. For the magnetic field measurement, the instruments thus selects one of the two CPT resonance superpositions $N = 2$ or $N = 3$ depending on the angle provided by the fluxgate sensors (Pollinger et al., 2018). In the equatorial region the CPT resonance superposition $N = 3$ is used while toward the poles the CPT resonance superposition $N = 2$ is applicable (Pollinger et al., 2020). To better understand the structure of the FGM and CDSM data set, an illustrative example is given in Figure 3.

Magnetic disturbances from the magnetorquer action, Tri-Band Beacon (TBB) instrument operation, and boom deformation may be significant. Flags listed in Tables 2 and 3 should therefore be carefully considered when using the data for scientific studies. To help readers better understand them, Figures 4 and 5 illustrate how these disturbances can affect the Level 2 data. Since the magnetic disturbance is small relative to the background geomagnetic field, residual fields ΔF and $\Delta \mathbf{B}$ are used for this purpose. These are separately calculated by subtracting predictions of the CHAOS-6-x7 geomagnetic field model from the CDSM and FGM observations. The CHAOS-6-x7 model is derived from magnetic field observations of the Swarm, CHAMP, Ørsted and SAC-C satellites and ground observatories and can be considered as an appropriate reference model describing magnetic field contributions from the core, crust and the large-scale magnetosphere (Finlay et al., 2016).

Figure 4 shows the ΔF residual field of the scalar intensity from the CDSM (Figure 4a) and the three vector components (Figures 4b–4d) of the $\Delta \mathbf{B}$ magnetic field from the FGM2 for four half orbits (No. 027781,
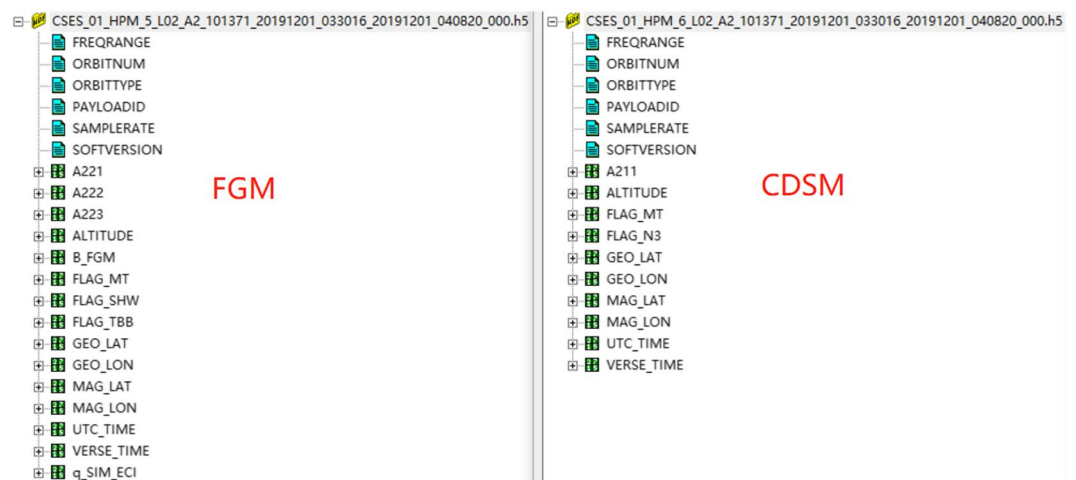

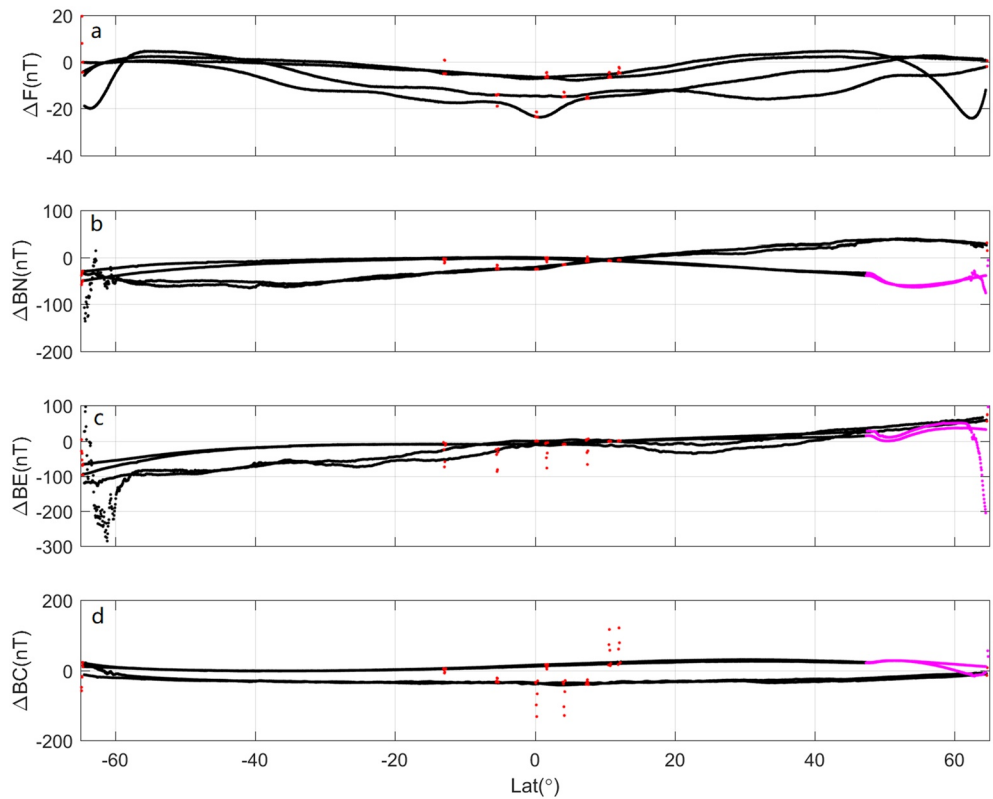**Figure 3.** Example of Level 2 FGM (left) and CDSM (right) data content.

Figure 4. Magnetic disturbances (as identified by their respective flags) due to magnetorquer activation (red dot) and deformation of the boom (magenta dot) when entering eclipse for four half orbits (No. 027781, 027790, 027791, 027800) on August 4, 2018. Shown are (a) the residual ΔF of the scalar intensity from the CDSM and (b–d) the three vector components (North, East, Center) of the ΔB residual from the FGM2.

027790, 027791, 027800) on August 4, 2018. Some outliers (see red dots) occur at low-latitudes and high-latitude around 65°. These outliers can reach up to several tens of nT in magnetic field intensity and more than 100 nT in the vector field. They are caused by magnetorquer activations, which are flagged by FLAG_MT with a value of "1" in the FGM and CDSM data. In Figure 4b and 4c, some "magnetic disturbances" around latitude ~50° are also seen. These are caused by boom deformation when CSES moves from sunlight to eclipse (ground shadow, highlighted by the magenta dot) and are signaled by a value of 1 in FLAG_SHW. As can be seen from Figure 4, these magnetic disturbances (red and magenta dots) can be accurately identified by the flags provided in the Level 2 data.
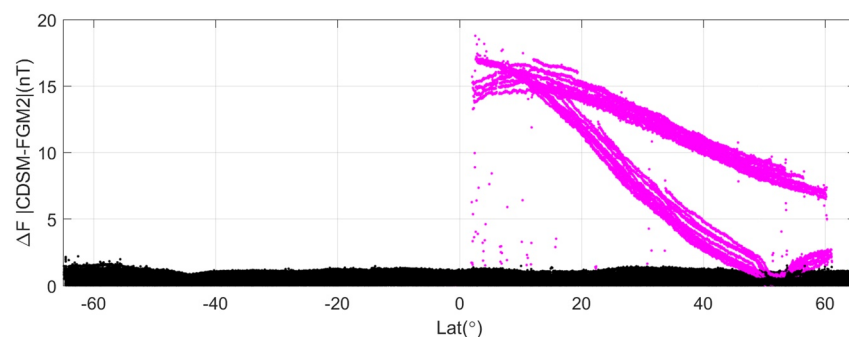

Figure 5. Residual field between CDSM and FGM2 during August 4–8, 2018. The magenta dots signal data flagged by FLAG_TBB = 1 as containing disturbances from the TBB.
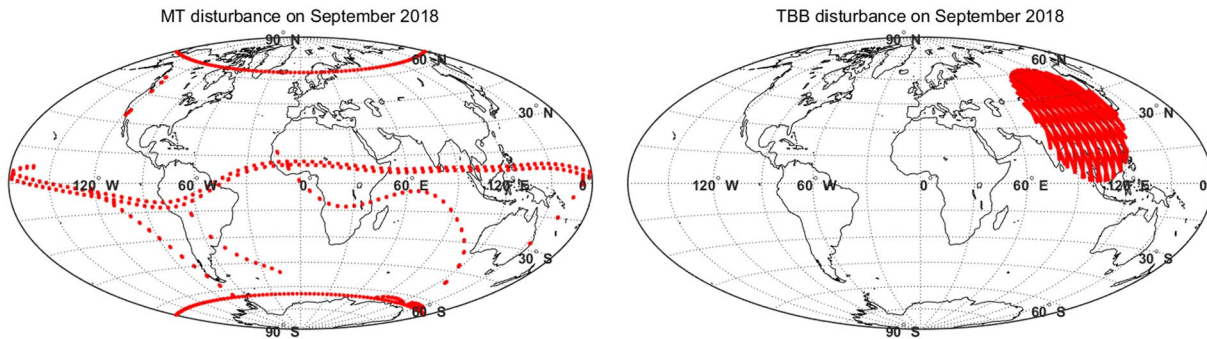
Figure 6. Magnetic field disturbance from MT (left) and TBB (right) during September 2018.

Figure 5 illustrates the difference in the scalar intensity between the CDSM and the modulus of the vector data provided by the FGM2 (after calibration) during August 4–8, 2018. By far the largest discrepancies to be seen are at northern latitudes between 0° and ~60° (as highlighted by the magenta dots). These reveal the signature of the magnetic disturbances produced by the TBB instrument when activated. During commissioning, indeed, it was found that the magnetic field vector measured by the FGM instruments (mainly the FGM2, less so the FGM1) is affected when the TBB is in operation, but not the total field measured by the CDSM. A correction model for this TBB disturbance is under development and will hopefully be implemented in the very near future. At present, we use FLAG_TBB = 1 to indicate the occurrence of such disturbances (the flag is set to FLAG_TBB = 0 when there is no TBB operation or the TBB is turned off). Figure 5 shows that such artificial disturbances range from a few nT to ~20 nT. We therefore advise users to also avoid using these flagged data for scientific studies.

To illustrate where such disturbances may occur, Figure 6 gives the geographic distribution of magnetorquer (MT, left) and TBB (right) disturbances (as identified by their respective flags) for the whole month of September 2018. As can be seen, disturbances from the TBB only occur above the Chinese territory. This is because the TBB is activated only when in view of the ground receivers installed there to monitor the ionospheric total electron content (TEC) and scintillation activity. In contrast, disturbances from the MT mainly concentrate near the magnetic equator and latitudes around 65°. These are the locations where highly disturbing specific activations of the MT need to be operated (MT are used for satellite attitude control, and rely on magnetized cores that regularly need to be re-magnetized at specific locations along the orbits, to next properly predict and correct the perturbations they produce along the rest of the orbits).

3. Preliminary Comparison with Swarm Data

Around August 20, 2018, CSES and Swarm Alpha were flying close to each other in local time, providing an opportunity to make cross-comparisons of the magnetic fields measured by both satellites. Figure 7 shows observations from a day side orbit on August 20, 2018. As shown in Figure 7a, the local time of the two satellites is around 14:00 LT between latitudes 65° South and North. The residual field (observations minus CHAOS-6-x7 model) for the magnetic field intensity and the three vector components (in NEC frame) were calculated respectively for CSES and Swarm and presented as red and blue curves in Figures 7b–7e.

Figures 7b–7e show that the main trend of the residual field is consistent between CSES and Swarm Alpha. Some differences in the amplitude, however, can be found, especially at high-latitudes. These differences may be attributed to two possible causes. First, they may originate from the position discrepancy between CSES and Swarm. As can be seen in Figure 7a, the longitudinal distance between the two satellites nearly reaches 30° at high-latitudes. In the work of Olsen and Stolle (2016) (who used the two satellites Swarm Alpha and Charlie flying side by side with a longitude separation of about 1.4°), it was found that the gradient of the magnetic field intensity can exceed 10 pT/km at high-latitudes where ionospheric Polar Electrojets (PEJs) occur. According to this estimation, several tens of nT in the differences between CSES and Swarm at high-latitude may thus be expected. Second, as illustrated in Figure 2, the STR on CSES is installed on the body of the satellite, far from the HPM, which is installed at the tip of a boom. Thus, the long distance
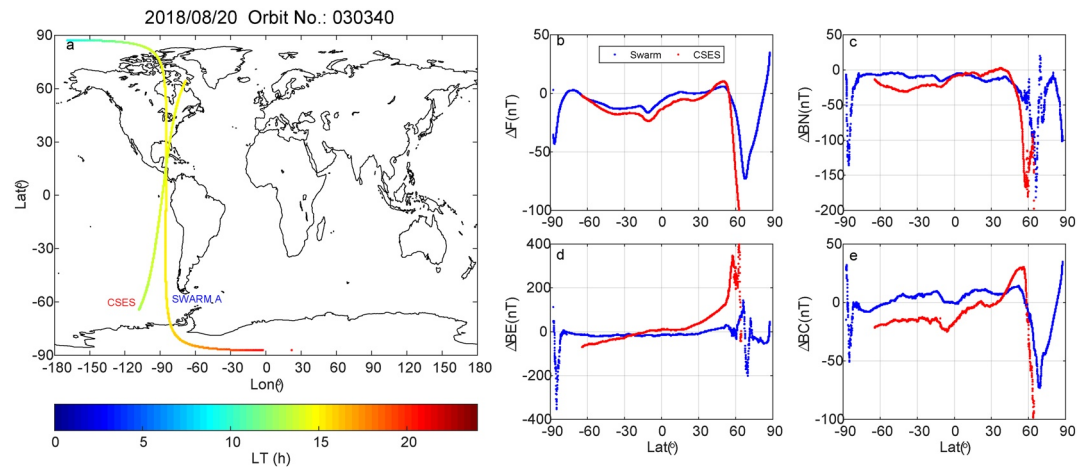
Figure 7. The residual field observed by CSES and Swarm from 1 day side orbit on August 20, 2018. Left (a): the local time distribution; Right (b): the residual magnetic field intensity; (c) north, (d) east, and (e) center components. Red and blue curves denote observations for CSES and Swarm, respectively, after removal of CHAOS-6-x7 model values.

between STR and FGM may cause some errors in the reconstruction of the NEC components of the FGM measurements because of possible boom deformation. According to our initial analysis, such deformations likely not only affect FGM vector components when entering in the shadow, but also between middle- and high-latitudes. In this specific event, the effect is more pronounced in the east component (see the red curve in Figure 7d) than in the other components. The comprehensive study of the uncertainties caused by the boom deformation is still ongoing and calibration will be further improved in the future. For the current version of data, one needs to keep this in mind and have a careful check when using FGM data.

Figure 8 further illustrates the comparison of the residual fields, now using more data from August 2018. Here we only concentrate on quiet time (Dst > −30 nT) observations, and remove data from the magnetic disturbed days of August 15–17, and 25–30, 2018. The residual field intensity and vector from CSES and
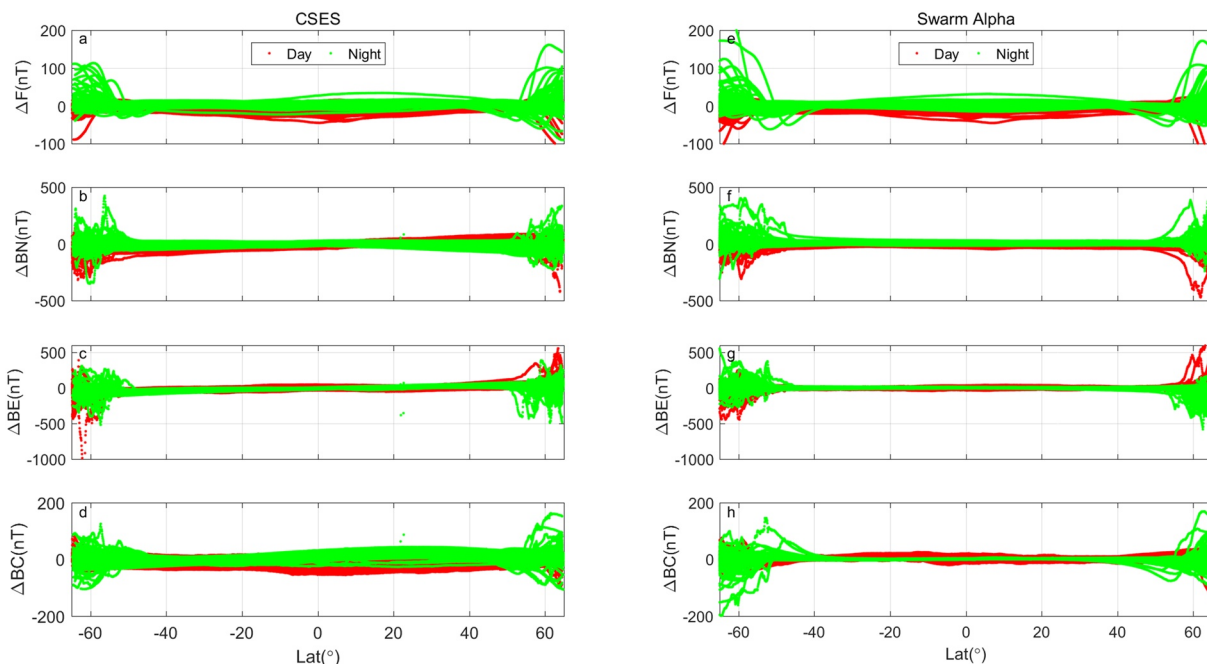

Figure 8. The residual field intensity (a and e) and vector (in NEC frame, b–d and f–h) comparison of CSES (left) and Swarm Alpha (right) during quite time of August 2018. The day time and night time results are respectively shown as red and green curves.

Swarm are respectively presented in the left and right columns of Figure 8. The red and green curves represent respectively the day and night time values. It can be seen that the results from the two missions display similar trends. However, Figure 8 also shows some differences in the three components of the two satellites. In particular, CSES displays a slow systematic variation with latitude, which is not seen in Swarm. In the case of the north component, for example, the residual field is maximum at high-latitude and minimum around the equator in day time. This trend is again possibly related to thermal deformations of the boom, which could also be the reason of the apparently larger day-to-day variability seen in the CSES center component, compared to that of Swarm. However, a detailed analysis is still ongoing and will hopefully lead to improved data in the future.

4. Response to an Intense Storm Event

Since the launch of CSES, several geomagnetic storm events have been observed. The largest event developed starting on August 25, 2018, with a minimum Dst reaching −174 nT at 07:00 UTC on August 26, 2018. In the following we used the Level 2 magnetic field data provided by the HPM instrument to check the magnetic signatures caused by this storm event.

The following residual field is considered to describe the magnetic field disturbance:

$$\Delta F = F_\text{o} - \left| \mathbf{B}_\text{core} + \mathbf{B}_\text{crust} \right|, \tag{2}$$

where F_o is the scalar field observation obtained with the HPM/CDSM instrument, and $\left| \mathbf{B}_\text{core} + \mathbf{B}_\text{crust} \right|$ are the scalar intensities of the sums of the core and crust fields predicted by the CHAOS-6-x7 model. Thus, ΔF represents magnetic perturbations attributed to current systems in the ionosphere and magnetosphere (and their solid-Earth induced counterparts).

Figure 9 shows the residual field for 15 selected descending (day time) orbits (numbered a–o) during August 25–27, 2018 (red). The observations from quiet time revisiting orbits during August 5–7 (green) are also introduced in the analysis as the reference before the storm, in order to identify any remaining static (core and crustal) field contributions. To make a comparison, ΔF from the Swarm Alpha satellite is also provided (blue curves in the figure). For each panel in Figure 9, UTC time, the corresponding Dst index and CSES orbit number on August 25–27 are also given. In the last panel of Figure 9, the orbit distribution from CSES (red) and Swarm (blue) is plotted.

Figure 9 indicates that all curves obtained on August 25 during quiet time (Figure 9a and 9b) are basically similar and the residual field values are less than a few tens of nT. During the storm, however, the residual field (solid red lines) has an obvious deviation from the quiet time, and behaves differently as the storm develops. For the initial phase (see Figure 9c and 9d), the residual field is slightly increased, reflecting the enhancement of the Dst index, before decreasing sharply to negative values during the main phase (as shown in Figures 9e–9i). The decreased residual field is proportional to the Dst value. For the recovery phase (Figures 9j–9o), however, the magnetic field perturbation becomes small. Another interesting feature in Figure 9 is that there is a clear enhancement of residual field at latitude around 50°N during the storm, not observed during quiet conditions. These features are related to enhanced Polar Electrojets (PEJs) during storm time.

In Figure 9, there is a slight additional local peak centered at 0° Quasi-Dipole (QD, Richmond, 1995) latitude (e.g., Figures 9e, 9f, 9i, and 9n), which reflects the signature of the dayside eastward Equatorial Electrojet (EEJ). Sometimes, however, a westward Equatorial Electrojet can be seen (e.g., Figure 9m), which is often known as a Counter Equatorial Electrojet (CEJ, e.g., Soares et al., 2018; Y.-L. Zhou et al., 2018). According to the statistical results of Y.-L. Zhou et al. (2018), such a dayside CEJ signature is more often observed during magnetic disturbed periods, due to the additional westward electric field at daytime at the equator caused by the disturbance wind dynamo (e.g., Blanc & Richmond, 1980; Scherliess & Fejer, 1997).

Figure 10 shows simultaneous observations from ground-based magnetometers and CSES and Swarm. To estimate the EEJ from the ground magnetic observatory data, we calculate the magnetic difference between two stations, for example, Huancayo (HUA, 12.05°S, 76.67°W) from Peru and Pilar (PIL, 31.4°S, 64.12°W) from Argentina (following the method used by e.g., Soares et al., 2018; Xiong et al., 2019). The CSES orbit
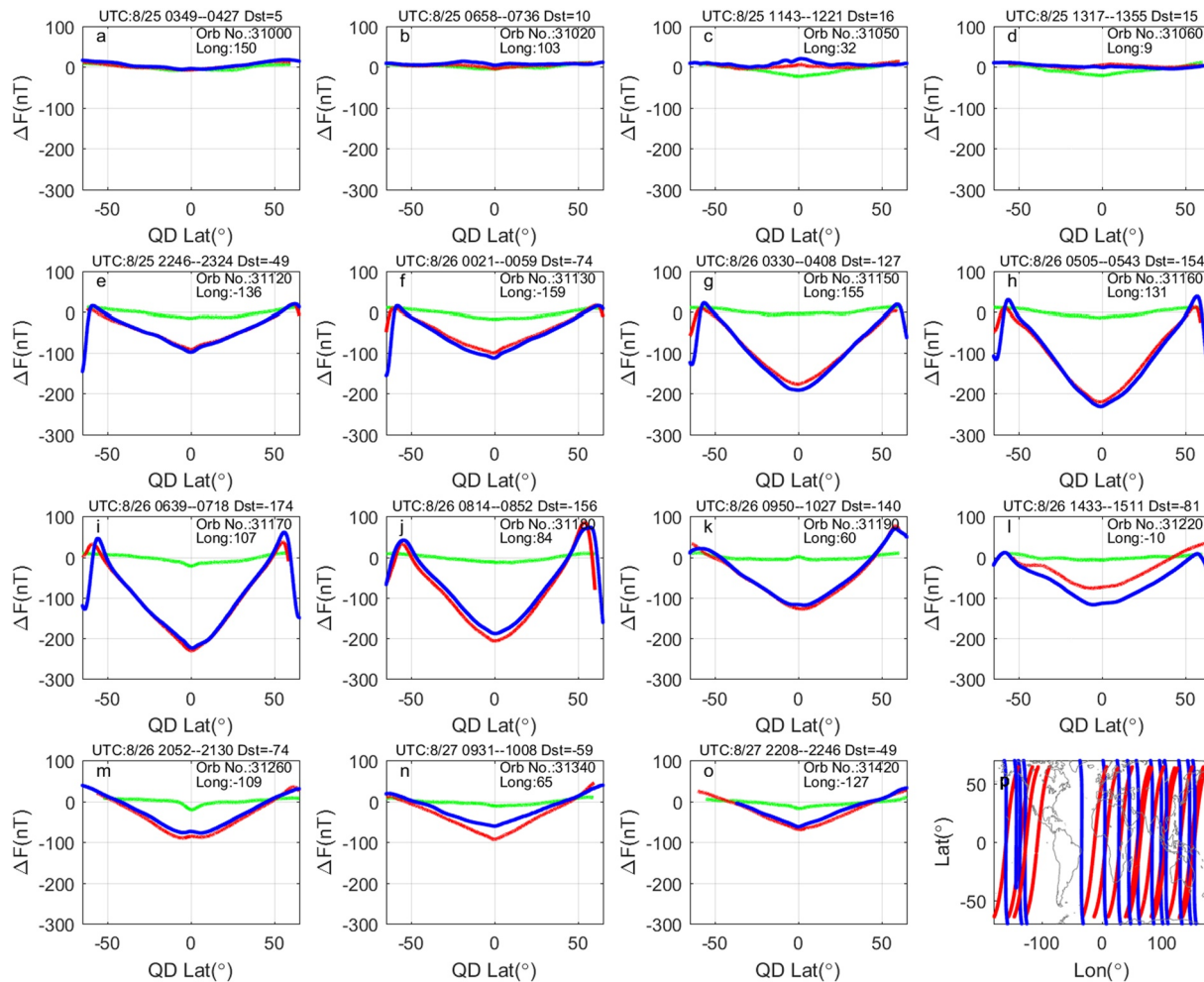
Figure 9. Residual field (observations minus CHAOS-6-x7 predictions) for 15 selected descending orbits (day time) during August 5–7 (green, before storm) and August 25–27, 2018 (red, during storm). Curves in each panel are revisiting orbits (similar ground tracks). The solid red curve represents magnetic perturbations attributed to current systems in ionosphere and magnetosphere. For comparison, Swarm Alpha residual fields attributed to ionosphere and magnetosphere perturbations are shown as blue curves. In each panel, UTC time, Dst index, CSES orbit number from August 25–27 and CSES longitude at QD lat = 0° are also provided. The last panel (p) displays the orbits of CSES (red) and Swarm Alpha (blue) for panels (a–o).

(No. 31240) on August 26 was found to be very close to the two stations. The locations of the chosen satellite orbit (red curve for CSES and blue curve for Swarm Alpha) and the two ground-based stations (red dots) are presented in Figure 10a. The magnetic equator is marked as the black curve. Figure 10b gives the magnetic field intensity difference of PIL and HUA. The green curve is the averaged values from quiet days (Dst > −30 nT), while the red curve denotes the variations on the storm day of August 26. Figure 10c shows the residual of the magnetic field intensity from the CSES and Swarm Alpha satellites. Both Figure 10b and 10c show that the EEJ is eastward during quiet time and turns to westward (CEJ) on August 26.

As discussed in many previous studies (e.g., Fejer et al., 1983; Xiong et al., 2015), prompt penetration electric field and ionospheric disturbance wind dynamo are two key factors controlling the variation of the equatorial zonal electric field. During southward interplanetary magnetic field (IMF) Bz conditions, the high-latitude convection electric field directed from dawn to dusk can penetrate down to the middle- and low-latitudes and enhance the dayside eastward EEJ. Meanwhile, the propagated equatorward winds from auroral to middle- and low-latitudes can generate a westward electric field on the dayside, that is, opposite to the regular eastward pattern. In general, the time-scale of prompt penetration electric field is quite short (less than an hour), while the enhanced equatorward wind takes 3–4.5 h to propagate from the high-latitude
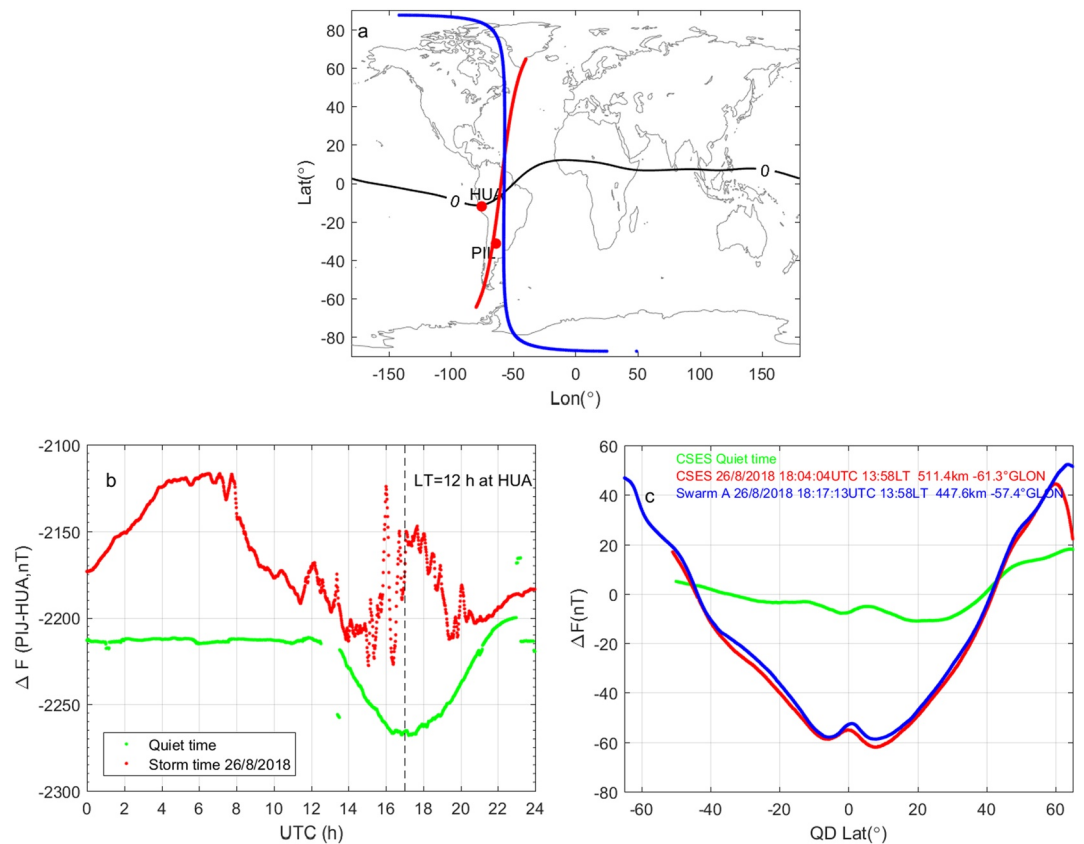
Figure 10. CEJ observed by CSES, Swarm Alpha and ground magnetic stations. (a) The location of HUA and PIL (red dots) and the selected CSES (red line) and Swarm (blue line) orbits. The magnetic equator is shown as a black line; (b) the magnetic field intensity difference between HUA and PIL. The green line denotes the average value from all quiet days in August, while the red line corresponds to the variations on August 26. The LT = 12h for HUA station is also shown by the vertical dashed line in panel b; (c) satellite magnetic residuals (blue for Swarm Alpha and red for CSES). The UTC time, LT, satellite height, and longitude at QD lat = 0° are also provided as insets. The green line is the CSES average value from four quiet time revisiting orbits in August (on August 1, 6, 11, and 21).

to the equatorial regions, due to inertia of neutral air (Xiong et al., 2015, 2016). The disturbance wind dynamo is most probably responsible for the westward electric field at the equator causing the CEJ.

Figure 11 now gives the residual field variation for ascending orbits during night time (02:00 LT). Generally, the main features are similar to those found during day time, with the magnetic field variation again showing large deviation during storm time (though somewhat less pronounced). Detailed discrepancies can nevertheless be found when comparing Figures 9 and 11. For example, there is no EEJ observed during night time, as shown in Figure 11. Furthermore, when comparing day side with night side observations, it is found that the amplitude of the night side residual field at high-latitude regions is stronger, indicating enhanced Polar Electrojet activity. An exemplary study on the potential interpretation of residual fields in terms of ionospheric currents along Swarm orbits has been conducted by Stolle et al. (2016).

Using FGM data, we also derive the field-aligned currents (FACs), j_{FAC}, based on Ampere's law. Theoretically, the full calculation of FACs can be achieved through simultaneous multi-point analysis, such as was done for ESA's Cluster mission (Escoubet et al., 2001). Estimations from a single-satellite, however, require a number of assumptions. Currents have to be assumed static over the time of spacecraft measurements and the sheet of FACs elongated approximately east–west and perpendicular to the satellite orbit (Lühr et al., 2020). Under these assumptions, FACs can be estimated by the following method (Lühr et al., 1996, 2020). We first calculate the radial component of the current by:
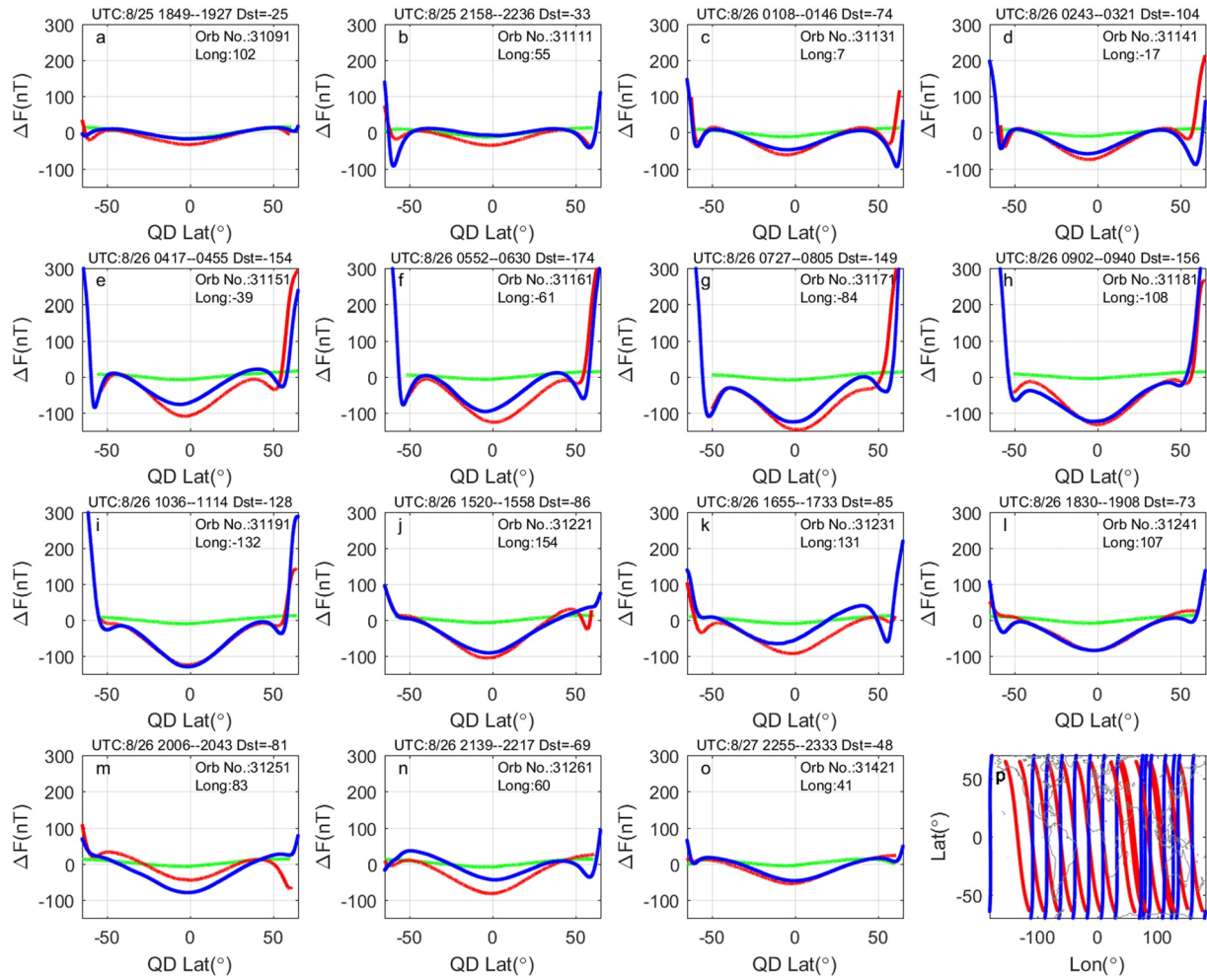
Figure 11. Similar to Figure 9, but for 15 selected ascending orbits (night time) during August 5–7 (before the storm, green line) and 25–27, August 2018 (during the storm, red and blue lines for CSES and Swarm Alpha respectively).

$$j_r = \frac{1}{\mu_0 v_x} \frac{dB_\phi}{dt}, \tag{3}$$

and then convert it to FACs by projection on the direction of the local magnetic field line:

$$j_{FAC} = j_r / \sin(I) \tag{4}$$

In Equations 3 and 4, $\mu_0 = 4 \times 10^{-7} H \cdot m^{-1}$ is the permeability of free space, I is the magnetic inclination, v_x is the northward spacecraft velocity and dB_φ is the residual of the eastward magnetic field (see also Equation 1) after removal of core, crustal and magnetospheric fields using the CHAOS-6-x7 model. Figure 12 shows the distribution of FACs in the Northern Hemisphere. The right figure gives the night side FACs for the orbit segment 31131 of CSES during August 26, 2018 during storm time (red curves). Observations from Swarm Alpha (from the Swarm Level 2 FAC product) at similar LT are also provided as blue curves. In the left figure, FACs from quiet time orbits during August 21, 2018 are shown. Finally, poleward and equatorward auroral boundaries predicted by the model of Xiong et al. (2014) as well as of Xiong and Lühr (2014) are also plotted (green curves).

From Figure 12, it can be seen that FACs observed from CSES and Swarm are in good agreement and can be used jointly to better reflect the movement of auroral boundaries. During the quiet time, the auroral boundaries (see green circles) are at very high-latitudes and the equatorward boundary is poleward of ∼65°
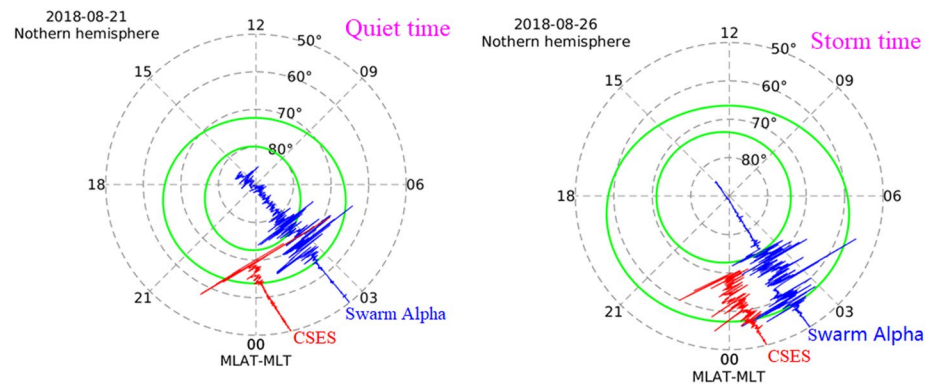
Figure 12. Northern Hemisphere nightside FACs observed by CSES (red) and Swarm Alpha (blue). Left: quiet time on August 21; Right: storm time on August 26. The two green curves are poleward and equatorward auroral boundaries derived from a statistical model based on CHAMP FAC data (Xiong et al., 2014).

magnetic latitude (MLAT). During the storm time, however, the boundary moves to lower latitudes and the equatorward boundary goes to below 60° MLAT. Interestingly, FACs deduced from CSES and Swarm are basically within the two boundaries, especially during storm times. CSES observations confirm that FACs indeed move equatorward during high magnetic activity. Previous studies have pointed out that latitudinal locations of FACs are generally at higher latitude for quiet times, while extend to lower latitude during strong activities (e.g., Iijima & Potemra, 1978; Xiong et al., 2014).

Using magnetic field intensity data, we can also produce estimates of the Dst index on an orbit-by-orbit basis. Figure 13 presents a CSES (in red) and Swarm Alpha (in blue) based Dst index from August 1–31, 2018, together with the ground-based determined Dst index (in black). To minimize ionospheric magnetic disturbance, only night time orbits are selected. Considering that the effect of the magnetospheric ring current is described by a $P_1 0$ spherical harmonic in dipole coordinates, it is better to use magnetic field variations at the dipole equator, therefore, for each orbit, the magnetic field data at dipole latitude 0° is chosen as the data set. Then, we use CHAOS-6-x7 model to remove core and crust field. Figure 13 indicates that the CSES and Swarm based Dst indexes (calculated by using the same approach as the ones used for CSES) well capture the main variations in the ground-based determined Dst index. It should be noted that the offset of 10–20 nT is expected since the ground-determined Dst index is relative to an unknown offset, while the satellite determined value has the correct offset. Indeed, ground-determined Dst is obtained from observatory data from which one has to remove non-magnetospheric contributions such as the core and lithospheric fields (and also ionospheric current contribution such as Sq and EEJ; note, however, that removal of ionospheric field contributions is ignored in the following discussion since we only use night time data for the calculation from CSES and Swarm). The core field can indeed be removed using a recent core field model, but the lithospheric field at ground observatories is poorly known due to local magnetic sources. In practice, contributions from core and
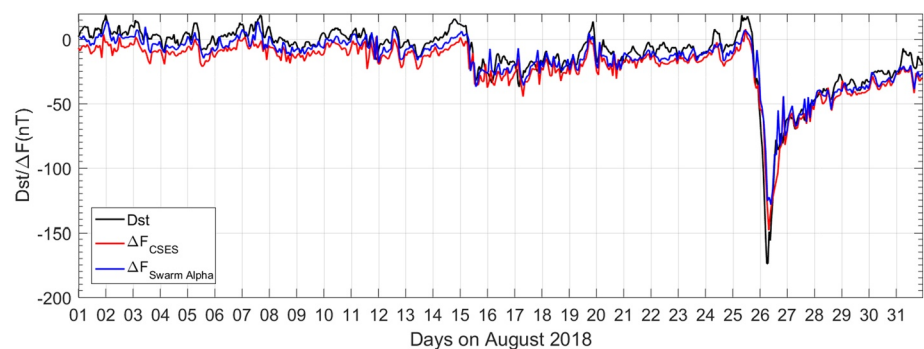

Figure 13. Dst index determined by ground observatory data (black) and the satellite-derived equivalent from CSES (red) and Swarm Alpha (blue) magnetic data between August 1 and 31, 2018.

lithospheric are removed from the ground observatory data by simply assuming that these are the only contributions during geomagnetic quiet times. Thus, by definition of the ground-determined Dst, the magnetic field disturbance during quiet conditions is forced to zero, which defines the practical baseline. Determination of the true baseline is only possible using satellite data, as first shown by Langel and Estes (1985), who found an offset in Dst of 20 nT. This is a typical value, which has been since confirmed using more recent satellites.

5. Summary

In this study, we first introduced the CSES HPM Level 2 data product to the scientific community. We then reported on a preliminary validation of the CSES HPM data using Swarm magnetic field measurement. Finally, some initial scientific observations obtained from HPM data during an intense magnetic storm event were discussed. The main findings can be summarized as follows:

(1) When dealing with HPM data, users should be aware that the magnetic field disturbances from magnetorquer action, operation of the TBB instrument and boom deformation, particularly when entering eclipse, which can cause disturbances up to 100 nT. Users should therefore carefully check the status of the flags (e.g., FLAG_MT, FLAG_SHW, FLAG_TBB) signaling data likely affected, or consult the authors, before carrying any scientific analysis
(2) The comparison between CSES and Swarm magnetic data shows that the observations from the two missions are quite close, indicating the good observational capability of CSES HPM. The complementarity of the high quality CSES and Swarm data makes them very useful for joint investigations of the magnetic signatures of geomagnetic storms
(3) CSES HPM observations show that the magnetic field variations in LEO behave differently on the day and night sides during intense storm events. At low and mid latitudes, the magnetic field variations on the dayside are larger than those on the nightside. At high-latitude, however, the situation is opposite, since Polar Electrojets are usually stronger during night time. On dayside, we also observe a clear CEJ signal during the recovery phase
(4) FACs calculated from CSES HPM data are comparable to those obtained from Swarm data and models, and clearly reflect the movement of FACs during storms. Using HPM data, we could also construct an analog to the Dst index, which displays a dynamics very close to that of the official Dst index

Generally, the preliminary analysis of CSES magnetic field data thus shows that the HPM package already provides data of good quality and high scientific potential. As a matter of fact, it is worth finally pointing out that a main field model has already been built using these CSES data (Yang et al., 2021), which successfully contributed to the latest release of the International Geomagnetic Reference Field model (Alken et al., 2021). We are now looking forward to many more such useful applications of the CSES HPM data.

Data Availability Statement

CSES data come from www.leos.ac.cn. Dst data originate from http://wdc.kugi.kyoto-u.ac.jp; Swarm data were downloaded from the FTP server https://swarm-diss.eo.esa.int. HUA and PIL observatory magnetic data is obtained from the INTERMAGNET website https://www.intermagnet.org/index-eng.php.

References

Alken, P., Thébault, E., Beggan, C. D., Amit, H., Aubert, J., Baerenzung, J., et al. (2021). International Geomagnetic Reference Field: The thirteenth generation. *Earth, Planets and Space*, *73*, 49. https://doi.org/10.1186/s40623-020-01288-x

Blanc, M., & Richmond, A. D. (1980). The ionospheric disturbance dynamo. *Journal of Geophysical Research: Space Physics*, *85*(A4), 1669–1686. https://doi.org/10.1029/ja085ia04p01669

Cheng, B., Zhou, B., Magnes, W., Lammegger, R., & Pollinger, A. (2018). High precision magnetometer for geomagnetic exploration onboard of the China Seismo-Electromagnetic Satellite. *Science China Technological Sciences*, *61*(5), 659–668. https://doi.org/10.1007/s11431-018-9247-6

Dolginov, S., Zhuzgov, L. N., Pushkov, N. V., Tyurmina, L. O., & Fryazinov, I. V. (1962). Some results of measurements of the constant geomagnetic field above the USSR from the third artificial Earth satellite. *Geomagnetism and Aeronomy*, *2*, 877–889.

Escoubet, C. P., Fehringer, M., & Goldstein, M. (2001). Introduction The Cluster mission. *Annales Geophysicae*, *19*(10–12), 1197–1200. https://doi.org/10.5194/angeo-19-1197-2001

Fejer, B. G., Larsen, M. F., & Farley, D. T. (1983). Equatorial disturbance dynamo electric fields. *Geophysical Research Letters*, *10*(7), 537–540. https://doi.org/10.1029/GL010i007p00537

Finlay, C. C., Olsen, N., Kotsiaros, S., Gillet, N., & Tøffner-Clausen, L. (2016). Recent geomagnetic secular variation from Swarm and ground observatories as estimated in the CHAOS-6 geomagnetic field model. *Earth, Planets and Space*, *68*(1), 18. https://doi.org/10.1186/s40623-016-0486-1

Friis-Christensen, E., Lühr, H., & Hulot, G. (2006). Swarm: A constellation to study the Earth's magnetic field. *Earth, Planets and Space*, *58*(4), 351–358. https://doi.org/10.1186/bf03351933

Hulot, G., Sabaka, T. J., Olsen, N., & Fournier, A. (2015). The present and future geomagnetic field. In G. Schubert (Ed.), *Treatise on Geophysics* (2nd ed., Vol. 5, pp 33–78): Oxford. Elsevier. https://doi.org/10.1016/B978-0-444-53802-4.00096-8

Iijima, T., & Potemra, T. A. (1978). Large-scale characteristics of field-aligned currents associated with substorms. *Journal of Geophysical Research*, *83*(A2), 599–615. https://doi.org/10.1029/JA083iA02p00599

Langel, R., Ousley, G., Berbert, J., Murphy, J., & Settle, M. (1982). The MAGSAT mission. *Geophysical Research Letters*, *9*(4), 243–245. https://doi.org/10.1029/gl009i004p00243

Langel, R. A., & Estes, R. H. (1985). Large-scale, near-field magnetic fields from external sources and the corresponding induced internal field. *Journal of Geophysical Research*, *90*(B3), 2487. https://doi.org/10.1029/jb090ib03p02487

Lesur, V., Wardinski, I., Rother, M., & Mandea, M. (2008). GRIMM: The GFZ reference internal magnetic model based on vector satellite and observatory data. *Geophysical Journal International*, *173*(2), 382–394. https://doi.org/10.1111/j.1365-246x.2008.03724.x

Lühr, H., Ritter, P., Kervalishvili, G., & Rauberg, J. (2020). Applying the dual-spacecraft approach to the swarm constellation for deriving radial current density. In M. W. Dunlop & H. Lühr (Eds.), *Ionospheric Multi-Spacecraft Analysis Tools*. ISSI Scientific Report Series (Vol. *17*, pp. 117–140). Switzerland: Springer Nature. Retrieved from https://doi.org/10.1007/978?3-030-26732-2_6

Lühr, H., Warnecke, J. F., & Rother, M. K. A. (1996). An algorithm for estimating field-aligned currents from single spacecraft magnetic field measurements: A diagnostic tool applied to Freja satellite data. *IEEE Transactions on Geoscience and Remote Sensing*, *34*(6), 1369–1376. https://doi.org/10.1109/36.544560

Maus, S., Rother, M., Stolle, C., Mai, W., Choi, S., Lühr, H., et al. (2006). Third generation of the Potsdam Magnetic Model of the Earth (POMME). *Geochemistry, Geophysics, Geosystems*, *7*(7). https://doi.org/10.1029/2006gc001269

Neubert, T., Mandea, M., Hulot, G., von Frese, R., Primdahl, F., Jørgensen, J. L., et al. (2001). Ørsted satellite captures high-precision geomagnetic field data. *Eos, Transactions American Geophysical Union*, *82*(7), 81–88. https://doi.org/10.1029/01eo00043

Olsen, N., Lühr, H., Sabaka, T. J., Mandea, M., Rother, M., Tøffner-Clausen, L., & Choi, S. (2006). CHAOS—a model of the Earth's magnetic field derived from CHAMP, Ørsted, and SAC-C magnetic satellite data. *Geophysical Journal International*, *166*(1), 67–75. https://doi.org/10.1111/j.1365-246x.2006.02959.x

Olsen, N., & Stolle, C. (2016). Magnetic signatures of ionospheric and magnetospheric current systems during geomagnetic quiet conditions—An overview. *Space Science Reviews*, *206*(1–4), 5–25. https://doi.org/10.1007/s11214-016-0279-7

Pollinger, A., Amtmann, C., Betzler, A., Cheng, B., Ellmeier, M., Hagen, C., et al. (2020). In-orbit results of the Coupled Dark State Magnetometer aboard the China Seismo-Electromagnetic Satellite. *Geoscientific Instrumentation, Methods and Data Systems*, *9*(2), 275–291. https://doi.org/10.5194/gi-9-275-2020

Pollinger, A., Lammegger, R., Magnes, W., Hagen, C., Ellmeier, M., Jernej, I., et al. (2018). Coupled dark state magnetometer for the China Seismo-Electromagnetic Satellite. *Measurement Science and Technology*, *29*(9), 095103. https://doi.org/10.1088/1361-6501/aacde4

Reigber, C., Lühr, H., & Schwintzer, P. (2002). CHAMP mission status. *Advances in Space Research*, *30*(2), 129–134. https://doi.org/10.1016/s0273-1177(02)00276-4

Richmond, A. D. (1995). Ionospheric electrodynamics using magnetic Apex coordinates. *Journal of geomagnetism and geoelectricity*, *47*(2), 191–212. https://doi.org/10.5636/jgg.47.191

Scherliess, L., & Fejer, B. G. (1997). Storm time dependence of equatorial disturbance dynamo zonal electric fields. *Journal of Geophysical Research*, *102*(A11), 24037–24046. https://doi.org/10.1029/97ja02165

Shen, X., Zhang, X., Yuan, S., Wang, L., Cao, J., Huang, J., et al. (2018). The state-of-the-art of the China Seismo-Electromagnetic Satellite mission. *Science China Technological Sciences*, *61*(5), 634–642. https://doi.org/10.1007/s11431-018-9242-0

Soares, G., Yamazaki, Y., Matzka, J., Pinheiro, K., Morschhauser, A., Stolle, C., & Alken, P. (2018). Equatorial counter electrojet longitudinal and seasonal variability in the American sector. *Journal of Geophysical Research: Space Physics*, *123*(11), 9906–9920. https://doi.org/10.1029/2018ja025968

Stolle, C., Michaelis, I., & Rauberg, J. (2016). The role of high-resolution geomagnetic field models for investigating ionospheric currents at low Earth orbit satellites. *Earth, Planets and Space*, *68*(1), 110. https://doi.org/10.1186/s40623-016-0494-1

Thébault, E., Finlay, C. C., Beggan, C. D., Alken, P., Aubert, J., Barrois, O., et al. (2015). International geomagnetic reference field: The 12th generation. *Earth, Planets and Space*, *67*, 79. https://doi.org/10.1186/s40623-015-0228-9

Xiong, C., & Lühr, H. (2014). An empirical model of the auroral oval derived from CHAMP field-aligned current signatures – Part 2. *Annales Geophysicae*, *32*(6), 623–631. https://doi.org/10.5194/angeo-32-623-2014

Xiong, C., Lühr, H., & Fejer, B. G. (2015). Global features of the disturbance winds during storm time deduced from CHAMP observations. *Journal of Geophysical Research: Space Physics*, *120*(6), 5137–5150. https://doi.org/10.1002/2015ja021302

Xiong, C., Lühr, H., & Fejer, B. G. (2016). The response of equatorial electrojet, vertical plasma drift, and thermospheric zonal wind to enhanced solar wind input. *Journal of Geophysical Research: Space Physics*, *121*(6), 5653–5663. https://doi.org/10.1002/2015ja022133

Xiong, C., Lühr, H., Wang, H., & Johnsen, M. G. (2014). Determining the boundaries of the auroral oval from CHAMP field-aligned current signatures – Part 1. *Annales Geophysicae*, *32*(6), 609–622. https://doi.org/10.5194/angeo-32-609-2014

Xiong, C., Lühr, H., & Yamazaki, Y. (2019). An opposite response of the low-latitude ionosphere at Asian and American sectors during storm recovery phases: Drivers from below or above. *Journal of Geophysical Research: Space Physics*, *124*(7), 6266–6280. https://doi.org/10.1029/2019ja026917

Yang, Y., Hulot, G., Vigneron, P., Shen, X., Zhima, Z., Zhou, B., et al. (2021). The CSES global geomagnetic field model (CGGM): An IGRF-type global geomagnetic field model based on data from the China Seismo-Electromagnetic Satellite. *Earth, Planets and Space*, *73*(1). 1–21. https://doi.org/10.1186/s40623-020-01316-w

Zhou, B., Cheng, B., Gou, X., Li, L., Zhang, Y., Wang, J., et al. (2019). First in-orbit results of the vector magnetic field measurement of the High Precision Magnetometer onboard the China Seismo-Electromagnetic Satellite. *Earth, Planets and Space*, *71*(1), 505. https://doi.org/10.1186/s40623-019-1098-3

Zhou, B., Yang, Y. Y., Zhang, Y. T., Gou, X. C., Cheng, B. J., Wang, J. D., & Li, L. (2018). Magnetic field data processing methods of the China Seismo-Electromagnetic Satellite. *Earth and Planetary Physics*, *2*(6), 455–461. https://doi.org/10.26464/epp2018043

Zhou, Y.-L., Lühr, H., Xu, H.-W., & Alken, P. (2018). Comprehensive analysis of the counter equatorial electrojet: Average properties as deduced from CHAMP observations. *Journal of Geophysical Research: Space Physics*, *123*(6), 5159–5181. https://doi.org/10.1029/2018ja025526